ACS APPLIED ELECTRONIC MATERIALS

pubs.acs.org/acsaelm Article

Electro-Optically Tunable Passivated Double-Cation Perovskite-Based ReRAM for Low-Power Memory Applications

Manvendra Chauhan, Ranbir Singh, and Satinder K. Sharma*

Cite This: ACS Appl. Electron. Mater. 2024, 6, 2709−2719 Read Online

ACCESS | Metrics & More | Article Recommendations | Supporting Information

ABSTRACT: 3-D Hybrid halide perovskites (HHPs) have garnered significant interest as a promising contender for next-generation resistive random access memory (ReRAM) technology. However, challenges such as variations in cycle-to-cycle switching iterations, operating voltages, and restrained reproducibility arise due to the disproportionate presence of grain size (GS) and grain boundaries (GBs), which are impediments to the widespread adoption of perovskite-based memory devices in commercial applications. Since GBs present in the thin film act as pathways for ion/cation migrations that eventually lead to the formation of conducting filament (CF), by regulating GBs, the resistive switching (RS) performance of the memory devices can also be improved. Herein, we initially optimized GS and thus GBs in the 3-D HHP thin film by the incorporation of FA^+ in the $MAPbI_3$ 3-D HHP to prepare double-cation 3-D $MAFAPbI_3$ HHP and determined that the doping of 10% FAI improved the $MAFAPbI_3$ film quality with an average grain size of ∼209.68 and 6.65 nm surface roughness, resulting in higher GBs that led to the stable RS of the fabricated Ag/$MAFAPbI_3$/FTO up to 491 cycles under dark conditions and 245 cycles under white light illumination with significantly low statistical variations (σ/μ %) in the consecutive switching cycles. This performance was achieved while maintaining low-resistance states (LRS) and high-resistance-states (HRS) ratios, i.e., LRS/HRS of ∼15.2 (dark) and ∼54.3 (white light) conditions at power consumption of ∼0.101 mW. Further, to improve LRS/HRS, the PEAI passivation layer was deposited over the optimized $MAFAPbI_3$ switching layer (SL) through spin-coating, and the fabricated Ag/PEAI/$MAFAPbI_3$/FTO ReRAM configuration exhibited LRS/HRS ∼10^5 at considerably low power, i.e., 0.12 and 0.23 mW while operating under dark and white light illumination, respectively. Furthermore, the RS mechanisms of Ag/$MAFAPbI_3$/FTO and Ag/PEAI/$MAFAPbI_3$/FTO were discussed and supported by the electrochemical metallization (ECM) model.

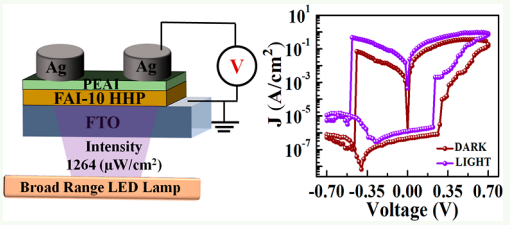

KEYWORDS: *perovskite based ReRAM, optoelectronic ReRAM, grain boundary*

1. INTRODUCTION

Low power consumption is a key consideration for electronic products/gadgets, especially battery-operated IoT devices, digital watches, medically implanted devices, etc. Such devices must ensure long battery life for reliable and durable operations. Most importantly, all such devices work on nonvolatile memories (NVM) to function as per the set protocols. However, NVM may not contribute as much to system power consumption as other components such as CPU, connectivity modules, or display, though integrating low-power NVM helps enable longer battery life, leading to improved energy efficiency and longer use times between recharging intervals. Nevertheless, NVM involves several elements that contribute to power consumption; most importantly, the read/write operations at high voltage (>5 V) lead to higher current conduction and thus result in high power consumption. Such issues were significantly eliminated through the ReRAM architecture. Particularly with the high-speed operations (sub ns) and low power consumption (sub-mW) ReRAM is a choice for next-generation NVM technology. The performance of the ReRAM majorly depends on the material integrated as a SL between the two electrodes.[1−6] Thereto, integrating the HHP as a SL into the ReRAM configuration is imperative due to its ability to engender read/write operations through executing SET/RESET in the current−voltage ($I-V$) hysteresis at low power in contrast to the metal oxides SL counterpart.[3−6]

Generally, the hysteretic behavior of a system is cognate with the variation in material properties due to external stimuli in electrical and optical fields.[7] More specifically, the properties associated with the perovskite materials, such as ion-migrations; trapping/detrapping of charge carriers, and metal cation (Ag^+ or Cu^+) movement across the perovskite layer from redox reactions of the active metal electrode, are said to be an accountable factor for hysteresis in perovskites.[3,4,8−11] Moreover, Snaith et al. have proven that the $I-V$ hysteresis strongly depends on the external triggering of the electric field,

Received: February 8, 2024
Revised: March 3, 2024
Accepted: March 6, 2024
Published: March 18, 2024

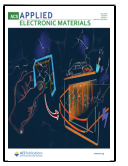

https://doi.org/10.1021/acsaelm.4c00257
ACS Appl. Electron. Mater. 2024, 6, 2709−2719

voltage sweep rate, and direction.[12] To date, most reports based on HHP memories have focused on the methylammonium iodide and formamidinium, single-cation (MA^+ and FA^+) e.g., $CH_3NH_3PbI_3$; $MAPbI_3$ and $CH_3(NH_2)_2PbI_3$; $FAPbI_3$ systems. It substantiated that I^- and MA^+/FA^+ can migrate under the influence of external fields owing to their low activation energy and result in $I-V$ hysteresis.[5,6,13,14]

Moreover, HHPs and $MAPbI_3$ also showed phototunable synaptic and RS behavior,[15,16] owing to alterations in physical and chemical properties such as tunable bandgap,[17] ambipolar charge transport,[18] long diffusion length,[19] and low trapping density[19] suitable for a broad range of optoelectronic device applications. Eminently, the incorporation of $MAPbI_3$ HHP as SL in the ReRAM architecture contributes to the development of optical and electrically active neuromorphic devices. Particularly, in optical neuromorphic devices, light stimulation drives the high-speed, high-bandwidth, and low-crosstalk neuromorphic systems over the electrical pulses.[20] Moreover, the optical neuromorphic devices are more energy-efficient (~sub pico joule) than the electrical neuromorphic devices (~few nano joules).[21] Due to the anticipated advantages of optoelectronic devices and optical neuromorphic architecture, and the ease of photoactive HHP material processing, this could be a possible SL for the realization of high-performance opto-memristor applications. Nevertheless, the evolution of HHP-based RS memory technologies is more challenging due to processing concerns; likewise, hygroscopic nature or moisture-induced deterioration and thermal stability of $MAPbI_3$, to which the organic components break down into HI and CH_3NH_2 and produce PbI_2, pose severe device reliability issues. One way to improve the thermal stability is to substitute $FA^+[HC(NH_2)_2^+]$ for $MA^+(CH_3NH_3^+)$. The primary issue with using $FAPbI_3$ is room-temperature structural instability since it can crystallize into two moisture susceptible phases: the yellow hexagonal (δ) phase and the black (α) trigonal phase.[22] Recent research has revealed that mixed-organic-cation hybrid perovskites $(MA)_x(FA)_{1-x}PbI_3$ are thermodynamically more stable at room temperature and preserve the superior properties of the pure FA material.[23] According to ab initio calculations, mixed-phase stability exists because they have greater entropies and lower formation enthalpies than the mixed δ-$FAPbI_3$ phase.[24] First and foremost, the RS characteristics of the double cation (e.g., $MAFAPbX_3$)-based ReRAM depend entirely on the doping concentration of cations at the A′-site of the $AA'BX_3$ perovskite structure. Recently, George and Vadivel Murugan[25] examined the electrical and optical switching characteristics of multiple double-cation perovskites prepared through the microwave-assisted solvothermal route, where $MAFAPbI_3$ exhibits set voltage (V_S) and reset voltage (V_R) of 0.5 and −1.7 V, respectively, in dark conditions and V_S/V_R of 0.3/−0.7 V under light illumination. However, optimum cation doping into the $AA'PbI_3$ lattice is still a challenge, and systematic investigations related to the effect of doping on RS current−voltage hysteresis, endurance variability, and retention are inferior. In addition, to develop a reliable RS memory device that uses HHPs as SL, it is critical to control the GS and GBs in the HHP thin films. In RS memories, the movement of ions/cations is largely facilitated through the GBs and helps in RS conduction.[26] The superlative control over the GS and GB morphology will enhance the RS memory window.[27,28] Therefore, the methodology followed to control the GS and GBs in HHP films is most likely related to the film deposition processes, choice of antisolvent, passivation layer, etc.[27,29] The doping concentration of cation/s at A-site or B-site can also regulate the GS and GBs.[30] Moreover, the size of the doped cation(s) also affects the local crystal orientation and threshold voltage besides providing moisture stability and a longer self-life to the HHP. The local crystal misorientation arises from the ionic size mismatch between the A-site cation and PbI_6 cage, which causes local lattice strain. Such lattice strain generates inhomogeneous defects and also reduces the formation energy of the lead iodide antisites, which further corresponds to the stochastic distribution of halide vacancies across HHP film, leading to larger variations in the electrical characteristics of the perovskite-based electronic devices.[31−33] Hence, it is crucial to investigate the precise doping concentration of cations in the HHPs to achieve reliable switching characteristics at optimal operating voltage in RS memories, along with some improvements toward moisture and air stability.

However, it is well known that the solution-processed perovskite films are usually polycrystalline; therefore, even after following GS and lattice strain optimization of the solution-processed 3-D HHPs system, they remain susceptible to moisture degradation owing to the presence of surface defects and uneven stoichiometry of the grains present in the 3-D HHP thin films.[34] In order to address these problems, a number of effective surface passivation techniques have been used recently. These techniques include the use of organic insulating layer coatings, such as polystyrene, poly(methyl methacrylate) (PMMA), and poly(ethylene glycol) (PEG),[35,36] as well as 2-D perovskite materials, like PEA_2PbI_4, to passivate trap states that are present on the surface of 3-D perovskite films, creating a 2D−3D structure.[37]

In contrast to 2D perovskite-coated 3-D HHP surfaces, organic phenethylammonium iodide (PEAI) salt has recently been shown to be an effective layer for 3-D HHP passivation application.[38,39] PEAI suppresses the defect states and rough morphology of the underneath HHP thin film surface in addition to offering significant stability against moisture and air degradation. This improves the electrical and optical properties of the devices that incorporate the PEAI/3-D HHP configuration.[38,39]

Also, to the best of our knowledge, the electro-optical RS characteristics of PEAI-passivated double cation $MAFAPbI_3$ prepared by the most convenient and straightforward route, i.e., the solution process, have not been explored yet.

In this regard, this work systematically investigated the opto-tunable RS functionality of PEAI-passivated 3-D $MAFAPbI_3$ HHP SL, i.e., PEAI/$MAFAPbI_3$ structure-based ReRAM devices in dark conditions and white light illumination, where HHP $MAFAPbI_3$ and PEAI-passivating layers were prepared through a cost-effective facile solution process route. Prior to examining the optoelectrical RS performance of PEAI/$MAFAPbI_3$-based ReRAM, the $MAFAPbI_3$ HHP SL is precisely optimized by controlling the GS of the HHP SL by regulating the doping concentration of FA cation in the MAFAPbI3 HHP. To establish the understanding of the role of FA cation concentration in the perovskite SL for resistive behavior, three sets of devices were fabricated, namely D1, D2, and D3, where D1 ReRAM incorporated $MAPbI_3$ (i.e., 0% FAI doping) SL sandwiched between the Ag top electrode (TE) and the FTO bottom electrode (BE). Similarly, D2 contained $MAFAPbI_3$ with 10% FAI doping, while D3 incorporated $MAFAPbI_3$ with 30% FAI doping. For all three sets of devices,

https://doi.org/10.1021/acsaelm.4c00257
ACS Appl. Electron. Mater. 2024, 6, 2709−2719

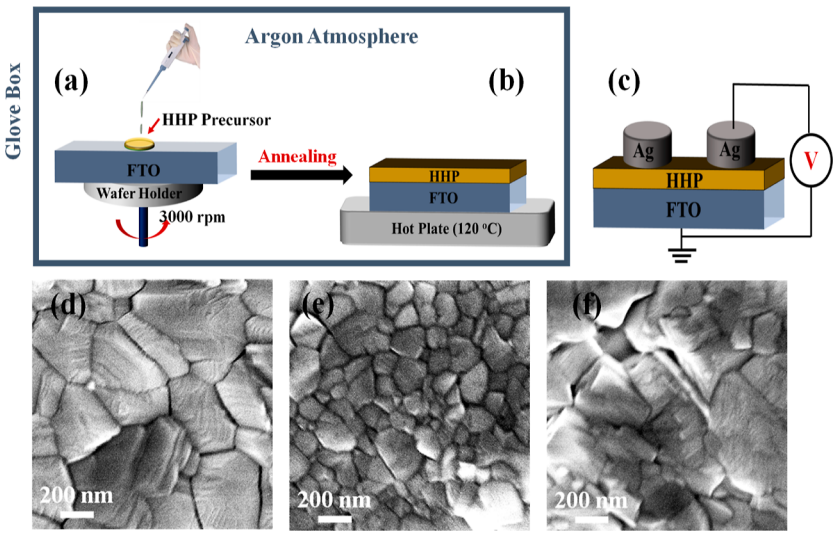

Figure 1. Schematic illustration of the fabrication of HHP-based ReRAM device as (a) HHP precursors (FAI-0), (FAI-10), and (FAI-30) spin-coated over FTO (BE), (b) annealing of spin-coated thin film of HHPs at 120 °C, (c) electrical characterization setup after Ag (TE) deposited over HHPs layer, and plain view SEM images of HHPs deposited over FTO (BE) (d) FAI-0, (e) FAI-10, and (f) FAI-30.

Ag and FTO were chosen for TE and BE, respectively. Later, the best of the three sets of fabricated ReRAM devices was tested under broad range white-light illumination. Subsequently, the effect of PEAI passivation of the optimized $MAFAPbI_3$ SL (i.e., FAI-10) on the RS performance of the ReRAM has been explored by fabricating Ag/PEAI/FAI-10/FTO ReRAM architecture and testing under dark and white light illumination. Ag/PEAI/FAI-10/FTO ReRAM devices are termed D4 later in this work.

2. RESULTS AND DISCUSSION

RS memory sets of devices D1, D2, and D3 were fabricated using organic−inorganic HHPs with FAI doping varying from 0 to 30% in the intrinsic $MAPbI_3$ HHP formulation. The prepared formulations were spin-coated over FTO and annealed at 120 °C in an argon environment inside the glovebox, as shown in Figure 1a,b (for more details on HHP formulation and ReRAM device fabrication see the Experimental Section). As-prepared HHP thin films with varied concentrations of FAI, such as 0, 10, and 30%, are labeled as FAI-0, FAI-10, and FAI-30, respectively, for later discussions in this work. The GS and GBs of the deposited HHPs vary according to the FAI doping concentrations. Figure 1d−f shows top-view scanning field emission scanning electron microscopy (FESEM) micrographs of FAI-0, FAI-10, and FAI-30 HHP thin films, respectively. A noticeable variation in GS and GBs was observed. The average GS was measured under FESEM as 392.35, 209.68, and 365.71 nm for FAI-0, FAI-10, and FAI-30 HHP thin films deposited over FTO, respectively. Variations in GS strongly indicate that the presence of the FA^+ cation in the $AA'BX_3$ matrix, along with the relatively smaller MA^+ cation, have a pronounced impact on both GS and GBs in these HHP films. Indeed, the FAI-10 exhibits an average GS of 209.68 nm, which is the smallest in comparison to the GS obtained for FAI-0 and FAI-30. Consequently, FAI-10 HHP thin films comprise a larger number of GBs. However, GBs are known to facilitate conducting filament (CF) formation as vacancies or halide/metallic ions can diffuse more easily with lower activation energies at GBs than the other pathways in HHP films.[28,40] Additionally, due to the fact that the GBs contain only 1/2 of the chemical bonds, the activation energy required for ion/cation migration at the GBs is approximately ∼1/2 of the energy in the bulk of HHP material.[41] Also, the current density in HHP is related to the number of GBs because the change in current in HHP is attributed to ion/cation migration. The presence of a smaller number of GBs suggests that the availability of fewer paths in HHP film for ion migration leads to low HRS current density and may result in providing a higher LRS/HRS ratio[42] that connotes a larger GS, and fewer GBs may provide a larger memory window.[27,28]

The effect of FA^+ cation doping in the A′ site of $AA'PbI_3$ HHPs on the RS performances was studied by fabricating the ReRAM with the Ag/HHP/FTO configuration. Three distinctive HHP films, namely FAI-0, FAI-10, and FAI-30, were processed through the facile solution route. To reveal the memory performance, all the fabricated HHP-based ReRAM devices, i.e., D1, D2, and D3, were characterized in the standard clean room ambient using the Keithley 4200 parameter analyzer, where DC double sweep was applied to the Ag TE from −0.5 to 0.5 V and FTO BE was grounded. The experimental setup is shown in Figure 1c.

Figure 2 illustrates the RS characteristics and statistical variability of consecutive 100 DC cycles of ReRAM D1, D2, and D3. The $J-V$ characteristics shown in Figure 2a−c plotted for D1, D2, and D3, respectively, represent the bipolar RS. All the devices are form-free, and discrete switching was observed during DC sweeps. For the D1 ReRAM devices, as the positive DC voltage increases, the current density remains very low, and the device maintains its HRS. However, the current increases abruptly at 0.145 V, indicating the formation of CF; consequently, D1 switches to LRS, as shown in Figure 2a at V_S = 0.145 V. As the applied DC voltage sweeps toward negative polarity, a soft decrement is observed at −0.35 V and then gradually decreases until applied at −0.5 V, moving toward HRS. Here, −0.35 V can be dedicated as V_R for D1. Further, ReRAM device D2 was investigated with the same voltage sweep and observed that D2 reached LRS at a voltage slightly higher than D1, i.e., V_S = 0.18 V. The higher V_S for D2 as compared to D1 is attributed to the local lattice strain induced in the HHP after larger FA^+ cation inclusion into the intrinsic

https://doi.org/10.1021/acsaelm.4c00257
ACS Appl. Electron. Mater. 2024, 6, 2709−2719

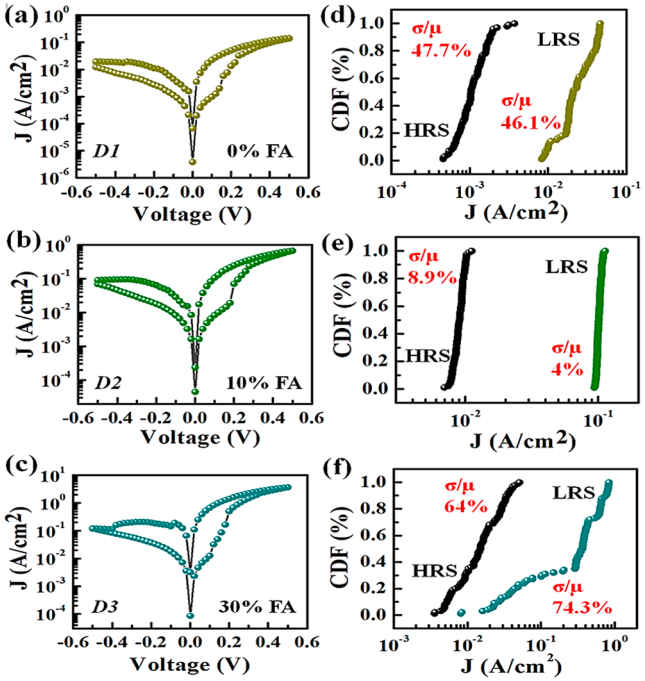

Figure 2. Resistive switching characteristics and cumulative distributive function percentage of corresponding LRS and HRS of (a,d) Ag/FAI-0 HHP/FTO, (b,e) Ag/FAI-10 HHP/FTO, and (c,f) Ag/FAI-30/FTO.

$MAPbI_3$ structure.[31−33] The introduction of such strain in the $MAFAPbI_3$ thin film facilitates the formation of internal defects, which, in turn, hinders charge carrier mobility.[43] This ultimately necessitates higher voltage levels for set operations in the device. As the negative voltage is applied to ReRAM device D2, the current density initially maintains its LRS up to −0.29 V and then starts decreasing gradually after reaching −0.30 V, which we are considering V_R for D2 (Figure 2b). The analog RS behavior during D2 at HRS conditions indicates the partial dissolution of the CF.[44] As the large cation FA doping increased up to 30%, more strain was induced in the intrinsic $MAPbI_3$ HHP structure; thus, a higher voltage was required to achieve LRS, which can also be observed in the semilog $J-V$ characteristics of D3 in Figure 2c. The V_S required for D3 to gain LRS is 0.185 V, which is the highest among the fabricated ReRAM devices D1 and D2, whereas it shows HRS level at a reset voltage of V_R = −0.38 V. The increment in operating voltages for D3 is attributed to the increment in lattice strain after 30% FA^+ doping, where the strain-induced structural defects dominate and readily affect the device threshold/operating voltage.[31,32] Also, such strain is known to alter the electronic band structure of the perovskite, thereby promoting a reduction in the effective mass of the charge carriers, so a comparatively higher current was observed in D3 ReRAM. All the device matrices are compared and shown in Table 1. Here, the LRS/HRS ratio obtained for ReRAM D2 is 10, whereas the LRS/HRS for D1 and D3 are 25 and 29, respectively. It shows that the larger GS of FAI-0 (∼392.35 nm) and FAI-30 (∼365.71 nm) HHP contributes toward lower HRS current density accordingly as afore-discussed, hence higher LRS/HRS in comparison to FAI-10 with the grain size of ∼209.68 nm.

Moreover, cumulative distribution function (CDF) percentages of LRS and HRS current density were calculated for each device considering the first consecutive 100 DC sweep cycles,

Table 1. ReRAM Characteristic Comparison of Fabricated Devices D1, D2, and D3

parameter	D1	D2	D3
SET/RESET voltage	0.145 V/−0.35 V	0.18 V/−0.30 V	0.185 V/−0.38 V
LRS/HRS ratio (@0.12 V)	25	15	29
statistical variation (%) in LRS/HRS	46.1/47.7	4/8.9	74.3/64

as shown in Figure 2d−f. LRS and HRS current densities for each device were compared at the same read voltage of 0.12 V for better comparison. The cumulative distribution of LRS and HRS was extracted to show the stability and variance in electrical parameters of ReRAM devices. The statistical variation σ/μ % is computed through the CDF (presented with red colored text in Figure 2d−f), where σ is the standard deviation, and μ is the mean. Here, statistical variation displays the inconsistencies and variabilities in consecutive LRS and HRS at constant voltage (i.e., 0.12 V) for each device. ReRAM devices presenting minimal σ/μ % (i.e., <10%) are only considered potential memory devices capable of delivering better overall performance. In this work, the device incorporating FAI-10 SL, i.e., D2 shows σ/μ % for LRS and HRS of 4 and 8.9%, respectively, which is highly appreciable and remarkable in terms of device stability in air. On the other side, ReRAM devices D1 and D3 show a very high percentage of variations in LRS and HRS current density. In the case of D1, significant variations of 46.1 and 47.7% in LRS and HRS current density are due to high surface roughness of ∼9.32 nm (Figure S1a). Whereas, the surface roughness measured for HHP incorporated in ReRAM D2, i.e., FAI-10, is 6.65 nm (Figure S1b). This suggests that the surface roughness also plays a vital role in the stability and performance of the RS characteristics. An optimized FAI-10 shows prominent behavior, whereas FAI-30, i.e., device D3, degrades the stability and shows the highest σ/μ % of 74.3 and 64% variation in LRS and HRS current density as the surface roughness increased up to 10.28 nm (Figure S1c). Hence, it can be concluded that improving the surface roughness of the SL by optimal doping of the FA^+ cation enhances the RS reliability of ReRAM devices. Additionally, as aforementioned, the introduction of local lattice strain in the HHP structure is more likely to enforce instability that corresponds to undesirable statistical variations if the concentration of doped cation is not precisely optimized.

Considering the best of the three sets of fabricated ReRAMs in terms of the low operating voltage, stability, and variance, i.e., D2 was tested under broad range white light illuminance of intensity 1264 $\mu W/cm^2$ (the UV−vis absorption spectra for FAI-10 HHP film are shown in Figure S2). All of the test conditions were kept similar to those mentioned above, except the light excitation. Figure 3a shows the schematic of the electrical characterization setup, and the ReRAM switching characteristics under the dark and white light are shown in Figure 3b. It indicates that under light illumination, D2 switches at a lower voltage of 0.10 V than a switching voltage of 0.18 V under dark conditions. Also, a difference can be observed in the LRS/HRS ratio. The LRS/HRS ratio for D2 under white light illumination is 54.3, which is 3.37 times higher than LRS/HRS under dark conditions. Hence, besides improving set voltage, D2 ReRAM also inherits a considerable memory window under white light excitation, while V_R slightly increases to −0.33 V under illumination. This enhancement in

https://doi.org/10.1021/acsaelm.4c00257
ACS Appl. Electron. Mater. 2024, 6, 2709−2719

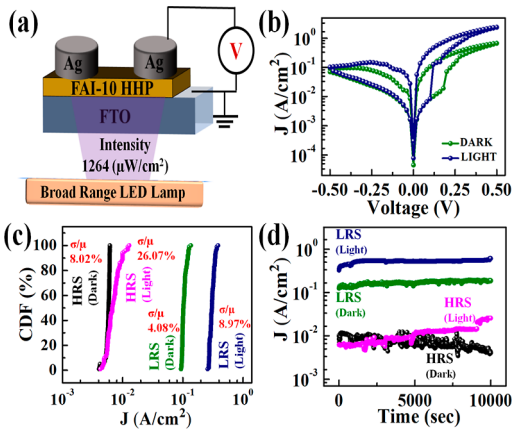

Figure 3. (a) Schematic illustration of the experimental setup for ReRAM D2 (Ag/FAI-10/FTO) electrical characterizations under dark as well as white light illumination, (b) resistive switching characteristics of optimized ReRAM D2 under dark conditions and white light illumination, (c) cumulative distributive function percentage of corresponding LRS and HRS of D2 under dark and white light excitations (statistical variation percentage written in red color), and (d) retention characteristics of ReRAM D2 under dark conditions and white light excitation.

RS properties of D2 under white light illumination is attributable to the illumination-induced spontaneous generation of electron−hole pairs in the FAI-10 HHP SL.[45] The reduced V_S under white light illumination suggests the quick induction of photocarriers, which promptly contributed in lowering the set voltage. However, the random movement of ions and cations under illumination results in a strong built-in electric field, necessitating a higher V_R to dissolve CFs.[46] Moreover, the fabricated Ag/FAI-10/FTO ReRAM (i.e., D2) exhibited significantly low-power consumption. During the SET operations under dark conditions and light illumination, D2 ReRAM consumed ∼0.101 mW. Hereto, the RESET process dissipated power of 0.021 and 0.0329 mW, respectively, while operating under dark and light conditions.

The reliability and stability of the D2 ReRAM were tested at 0.12 V read voltage under dark conditions through DC endurance, where it maintains LRS/HRS ∼15.2 up to 491 DC cycles, as shown in Figure S3a. In contrast, it upheld LRS/HRS ∼54.3 up to 245 DC cycles when illuminated under white light, as shown in Figure S3b. The excess electrons generated under the continuous white light illumination hinder the CF formation as there is the possibility of Ag^+ getting reduced to the Ag atom by accepting the photogenerated electrons without reaching the BE. This might be the reason that D2 was able to sustain LRS/HRS ∼54.3 only up to 245 DC cycles and then started to degrade. The CDF % have also been calculated for D2 under white light excitation considering 100 consecutive DC cycles and was compared with the same for dark, as shown in Figure 3c. It was observed that the illuminated light over perovskite degrades its stability as iterations increase. This might be due to the excess electron−hole pair generation near the BE and the perovskite interface that also contributes to the stochastic distribution of the halide ion under the electric field, resulting in uncontrolled halide vacancy movements across the switching layer and accumulation near the TE or BE, in addition to Ag^+ movements. Table 2 compares the switching parameters of D2 under dark and light conditions. The retention data was plotted for ReRAM

Table 2. ReRAM Characteristic Comparison of the Fabricated D2 Device under Dark and Light Conditions

parameter	D2 (under dark)	D2 (under light)
SET/RESET voltage	0.18 V/−0.30 V	0.10 V/−0.33 V
LRS/HRS ratio (@0.12 V)	15.2	54.3
statistical variation (%) in LRS/HRS	4.08/8.02	8.97/26.07

D2 under dark conditions as well as white light excitations, as shown in Figure 3d. The device was tested up to 10^4 s, and it can be observed that the fabricated ReRAM D2 follows an LRS/HRS current density ratio of ∼15.2 under the dark condition, and the LRS/HRS ratio improved to ∼54.3 when excited under white light and maintained it for 10^4 s with negligible changes.

Understanding the resistive switching mechanism of the Ag/FAI-10 HHP/FTO device is crucial. To investigate this mechanism in detail, typical current density−voltage (J−V) curves plotted in a double-logarithmic scale for both set (positive DC sweep) and reset (negative DC sweep) operations are shown in Figure 4. The slope values for the HRS and LRS were determined by fitting the log J vs log V curves linearly, utilizing the analogy of the power relation ($J \alpha V^n$).[35]

The double log J−V curves of D2 in positive and negative voltage regions under dark conditions are shown in Figure 4a,c, respectively. Initially, D2 was in HRS under the positive voltage sweep with a low applied field ($0 < V < 0.14$) and a slope of ∼1.03 indicating ohmic conduction ($I \alpha V$), where the current was controlled mainly by thermally excited electrons in the conduction band.[47] Later, the slope increases as ∼1.78 under the voltage region $0.14 < V < 0.18$, indicating nonlinear growth of the current following space charge limited conduction (SCLC) ($I \alpha V^2$) attributed to the migration of Ag^+ from the Ag TE toward the counter BE, i.e., FTO via GBs presented in the FAI-10 SL. As the voltage increases, more Ag atoms are oxidized to Ag^+ ions as $nAg \rightarrow Ag^{n+} + ne^-$.[48] These generated Ag^+ ions were reduced near the BE as $Ag^{n+} + ne^- \rightarrow nAg$[48] and grew toward the TE, providing multiple conducting channels as shown in Figure 4b. This eventually led to a sharp jump in the device current, reaching the LRS at $V_S = 0.18$ V, confirming the formation of Ag CFs. Such a very low V_S requirement for Ag/FAI-10/FTO ReRAM is ascribed to the higher GBs and lower energy barrier for Ag diffusion[49] in the FAI-10 SL. A steady FAI-10 host environment would aid in maintaining the multiple CF formed through GB networks present in the FAI-10 HHP SL and extending the retention duration after it has been adequately formed across the SL. Further, an increment in the voltage ($V > 0.2$) leads to the charge hopping phenomenon arising due to the halide vacancies (I_O) randomly generated across the SL facilitating the charge trapping/detrapping conduction, as indicated by slope ∼3.27 in Figure 4a, and thereafter, the current with the slope ∼1.77 shows quadratic growth up to the applied 0.5 V and then decreases linearly while returning to 0 V with the slopes ∼0.97 ($0.5 > V > 0.22$) and ∼1.15 ($0.22 > V > 0$). The ohmic conduction was then retained during a negative DC sweep until the device reached $V_R = -0.30$ V. Thereafter, the device transitioned to HRS conduction with the fitted slope ∼0.27 ($I \alpha V^{1/2}$) as shown in Figure 4c, confirming the presence of a barrier near the BE and SL interface. The large accumulation of halide ions (I^-) at the BE under the high voltage region ($V \geq -0.30$) contributes to the formation of a

https://doi.org/10.1021/acsaelm.4c00257
ACS Appl. Electron. Mater. 2024, 6, 2709−2719

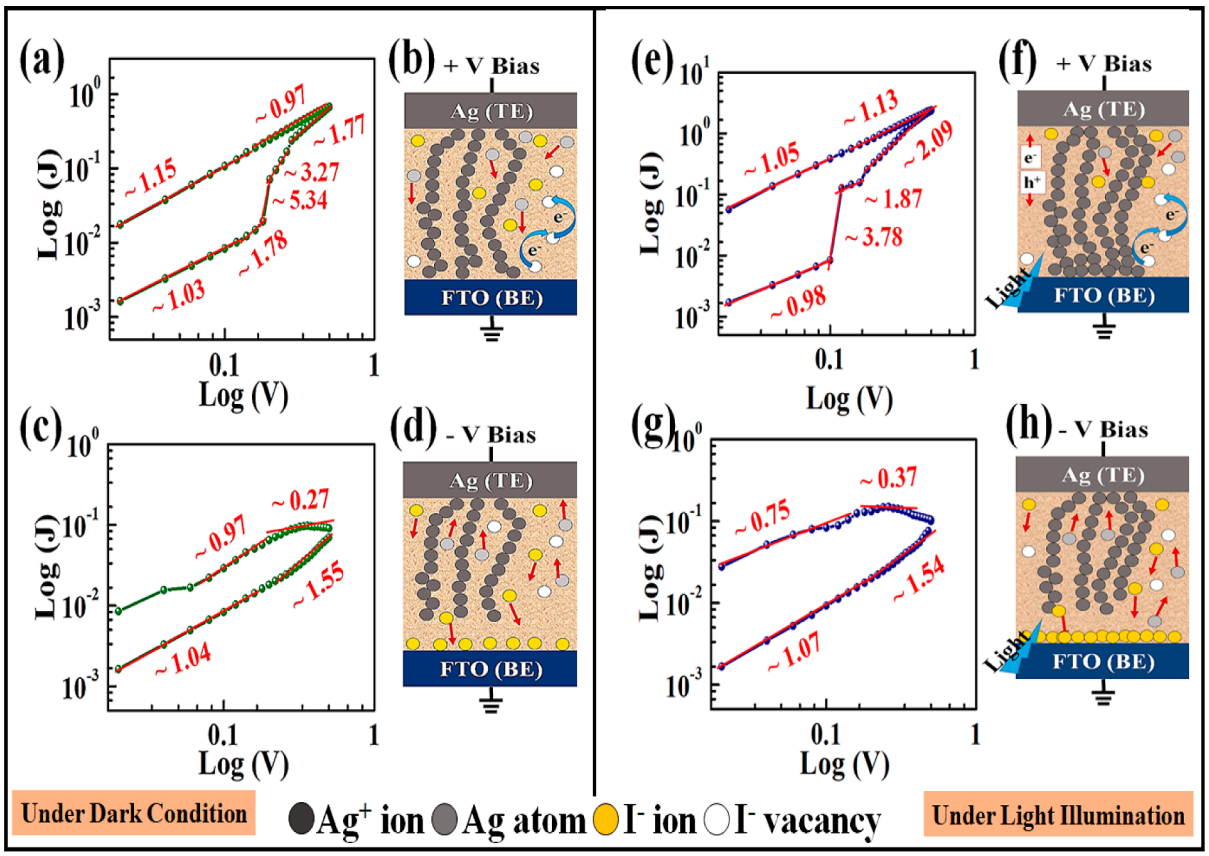

Figure 4. Conduction mechanism of ReRAM D2 under dark conditions: (a) log–log J–V curves for the positive voltage sweep region with the linear fitting, (b) schematic illustration of the possible LRS switching mechanism, (c) log–log J–V curves for the negative voltage sweep region with the linear fitting, (d) schematic illustration of the possible HRS switching mechanism; and the conduction mechanism of ReRAM D2 under light illumination, (e) log–log J–V curves for the positive voltage sweep region with the linear fitting, (f) schematic illustration of the possible LRS switching mechanism, (g) log–log J–V curves for the negative voltage sweep region with the linear fitting, and (h) schematic illustration of the possible HRS switching mechanism.

Schottky barrier[50] at the BE/SL interface and thus blocks the carrier movement, which hinders the Ag^+ ions reduction to Ag atoms near the BE and leads to the rupturing of Ag CFs near the BE, as shown in Figure 4d.

Similarly, when D2 operated under white light illumination in the low voltage region (<0.1 V) of positive DC sweep, the double log J–V curve follows ohmic conduction (slope ~0.98) as shown in Figure 4e, and then it showed nonlinear growth. The nonlinear growth is attributed to the photogenerated electron–hole pairs (e^-–h^+). These photoelectrons contributed to the current conduction along with the Ag CF formed at V_S = 0.10 V. Due to the external source, i.e., white light excitations, greater number of Ag atoms oxidized to Ag^+ and thus reduced more at BE, forming more Ag CF through existing GBs in contrast to the CF formed under the dark conditions. Hence, a higher current was observed during the LRS of D2. The current conduction mechanism of D2 (under white light) during the set operation is illustrated in Figure 4e. The device then follows ohmic conduction while returning to 0 V from its LRS, analyzed through the fitted slope of ~1.13 (0.5 < V < 0.22) and ~1.05 (0.22 < V < 0). Now, as the device structures operated under the negative bias region, the plotted double log J–V curve fitted with the slopes of ~0.75 (0 < V < −0.2) and ~0.37 (−0.2 < V < −0.33) (Figure 4g) suggests the presence of a stronger barrier near the BE as the voltage increases in the negative region due to a larger accumulation of I^- ions at the BE/SL interface. Here, the photon irradiation provides extra energy to the Pb–I, causing the early breakdown of Pb–I bond[25] to influence the large amount of I^- ion migration toward BE, resulting in the formation of Schottky barrier at the interface after heavy accumulation near BE. This Schottky barrier obstructs the growth of Ag CF and facilitates the dissolution of Ag CF near the BE; hence, D2 transitioned to HRS from LRS at V_R = −0.33 V. The V_R required to achieve HRS under white light illumination is higher than that of the devices operated under dark conditions because of the higher number of Ag CF, as more energy is required to dissolve multiple filaments. The formation and rupture of the Ag CF under white light illumination are depicted in Figure 4f,h, respectively. Hence, the present work suggests the emergence and dissolution of conducting Ag filaments in the FAI-10 SL, which also insinuates the RS mechanism of D2 ReRAM dominated by the electrochemical metallization (ECM) mechanism.[51] To verify the ECM in the experimental results, the Pt/FAI-10 HHP/FTO memory devices were fabricated by using inert Pt as TE (discussed in Supporting Information, under Section S4). From the semilog J–V curve, as shown in Figure S4, analog switching can be observed that confirms no CF formation in Pt/FAI-10 HHP/FTO ReRAM structures while sweeping DC voltages from −1 to 1 V and the double-log J–V verifies the charge trapping/detrapping mechanism shown in Figure S5. Therefore, it is safe to state that the formation and rupture of Ag CF are responsible for the RS

https://doi.org/10.1021/acsaelm.4c00257
ACS Appl. Electron. Mater. 2024, 6, 2709–2719

behavior of ReRAM D2, i.e., Ag/FAI-10 HHP/FTO ReRAM structures.

Nevertheless, the afore-investigated ReRAM configuration incorporating optimized FAI-10 HP SL exhibited ultralow operating voltages to SET and RESET ReRAM with marginal variations in consecutive switching, but it offers insignificant LRS/HRS of ∼15.2 and ∼54.3, respectively, when excited under the dark and white light illumination. Such a low LRS/HRS ratio indicates the following degrading factors involved in the perovskite SL: (i) the detrimental leakage current arises due to the presence of surface defects in the perovskite SL; (ii) variability in the switching mechanism attributed to the large number of Ag^+ diffusions in the SL through the Ag electrode; and (iii) degradation of the SL due to the presence of moisture in the testing environment. Therefore, in order to improve the LHS/RHS ratio, the optimized $MAFAPbI_3$ was passivated with the moisture-resistant phenethylammonium cation (PEA^+). Phenethylammonium cation (PEA^+) is recognized for uniform passivation of surface defects and trap states present on the HHP surface.[38] Hence, phenethylammonium iodide (PEAI) salt was dissolved in IPA and spin-coated over optimized $MAFAPbI_3$ (i.e., FAI-10). The plain-view SEM images and the AFM morphology of the PEAI-passivated FAI-10 HHP layer are shown in Figure S6a,b. After depositing PEAI over-optimized FAI-10 SL, the essential RS characteristics of the fabricated Ag/PEAI/FAI-10/FTO (i.e., D4) are investigated, as shown in Figure 5.

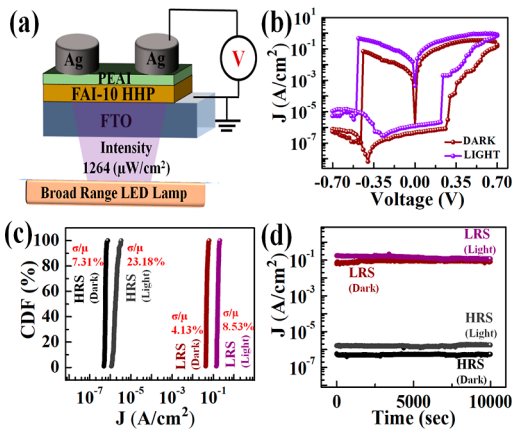

Figure 5. (a) Schematic illustration of the experimental setup for ReRAM D4 (Ag/PEAI/FAI-10/FTO) electrical characterizations under dark as well as white light illumination, (b) resistive switching characteristics of optimized ReRAM D4 under dark conditions and white light illumination, (c) cumulative distributive function percentage of the corresponding LRS and HRS of D4 under dark and white light excitations (statistical variation percentage written in red), and (d) retention characteristics of ReRAM D4 under dark conditions and white light excitation.

The fabricated D4 devices were examined under dark and white light illumination, as shown in Figure 5a, with cyclic DC voltage loops of −0.7 to +0.7 V and finally to −0.7 V. The RS characteristic, as shown in Figure 5b, indicates that the D4 ReRAM switches to its LRS at 0.26 and 0.22 V, respectively, under dark and white light excitation. It can be observed that the set voltage of D4 is slightly higher than the voltage required to set D2 ReRAM. This might be attributed to the passivation of GBs present in the FAI-10 HHP SL by PEAI layer deposition,[38] which restricts the convenient drift of the Ag^+ through the GBs under the positive electric field, and hence, comparatively higher voltage required to set D4 into LRS. In addition to GBs passivation, it also suppressed the surface defects present in the FAI-10 HHP SL,[39] which in turn benefits from very low leakage current during switching operations. Adjacent thereto, it also restrained the growth of Ag CF across SL,[52] which led to filament confinement in the SL and hence reduced the variability in the switching mechanism.[53,54] The application of the PEAI layer over the FAI-10 SL also acts as a barrier layer sandwiched between Ag TE and FAI-10 SL due to its high bandgap,[39] which eventually results in very low HRS current. Hence, it is safe to state that the significantly high LHS/RHS of $\sim 1.07 \times 10^5$ and $\sim 1.08 \times 10^5$, respectively, exhibited by ReRAM D4 (Figure 5b) under dark and white light illumination is ascribed to the PEAI layer passivation over FAI-10 HHP SL. Further, as the voltage sweep reaches the negative polarity, D4 attains its HRS at −0.44 V when operated under dark conditions, whereas −0.48 V is the reset voltage in the case of white light excitation. However, it consumed slightly more power in comparison to D2 ReRAM. During the SET operations under dark conditions and light illumination, D4 ReRAM consumed ∼0.12 and 0.23 mW, respectively.

For the reliability and stability analysis of the D4 ReRAM under dark conditions, a 0.12 V read voltage was applied for the DC endurance test. The fabricated D4 ReRAM maintains LRS/HRS $\sim 1.07 \times 10^5$ up to 4003 DC cycles, as shown in Figure S7a. In contrast, it upheld LRS/HRS $\sim 1.08 \times 10^5$ up to 2436 DC cycles when illuminated under white light, as shown in Figure S7b. This improvement in the endurance property of D4 is credited to the moisture-resistant PEAI passivation layer coated over FAI-10 HHP SL, which prevents its fast degradation while characterizing the device in a clean room atmosphere with a standard humidity of 41 ± 0.5%. Hereto, it exhibited 8.15 times higher stable consecutive switching cycles under the dark conditions and 9.94 times higher switching when excited through white light in comparison to the D2 ReRAM endurance. The CDF % calculated for D4 (Figure 5c) exhibits improved σ/μ % compared to D2. Also, the retention data tested for 10^4 s in the case of D4 ReRAM presents nearly uniform data dispersion throughout 10^4 s, with significantly marginal fluctuations (Figure 5d). Such astounding RS characteristics of D4 confirm that PEAI passivation over FAI-10 HHP SL played a significant role in suppressing the variabilities in the switching mechanism that were previously observed in the case of unpassivated D2 ReRAM.

Moreover, considerable enhancement in the reliability of the switching performance of the D4 ReRAM is attributed to the controlled CF growth across the SL. The deposited PEAI layer, with a large surface area of ∼1.94 nm roughness (Figure S6), completely filled the GBs present at the FAI-10 SL surface and hence blocked the stochastic diffusion of Ag^+ through the GB pathways. Consequently, the uncontrolled random formation of multiple Ag CFs stopped across the SL, promoting the confined growth of Ag CF reaching toward BE from Ag TE.[39] The formation and rupture of CF in the fabricated Ag/PEAI/FAI-10/FTO ReRAM, i.e., D4, under dark conditions and white light illumination, as illustrated in Figure 6.

The log−log $J-V$ curves of D4 in positive and negative voltage regions under dark conditions are shown in Figure 6a,c, respectively. Under the positive sweep ($0 < V < 0.26$), the device was initially at the HRS with a slope of ∼0.25, indicating Schottky emission ($I \alpha V^{1/2}$) dominates at such low applied

https://doi.org/10.1021/acsaelm.4c00257
ACS Appl. Electron. Mater. 2024, 6, 2709−2719

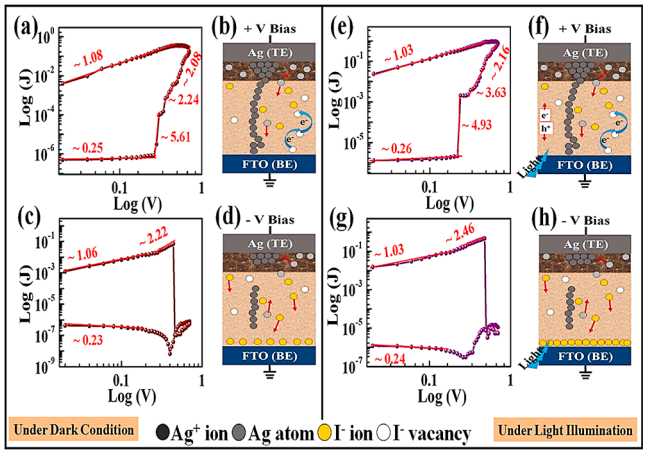

Figure 6. Conduction mechanism of ReRAM D4 under dark conditions: (a) log−log J−V curves for the positive voltage sweep region with the linear fitting, (b) schematic illustration of the possible LRS switching mechanism, (c) log−log J−V curves for the negative voltage sweep region with the linear fitting, (d) schematic illustration of the possible HRS switching mechanism; and the conduction mechanism of ReRAM D4 under light illumination: (e) log−log J−V curves for the positive voltage sweep region with the linear fitting, (f) schematic illustration of the possible LRS switching mechanism, (g) log−log J−V curves for the negative voltage sweep region with the linear fitting, and (h) schematic illustration of the possible HRS switching mechanism.

bias. As the voltage reached 0.26 V, D4 abruptly switched to a higher current level and attained its LRS at V_S = 0.26 V. The comparatively higher V_S in the case of ReRAM D4 is attributed to the single CF formation across the SL, as the PEAI layer efficiently impedes the Ag^+ migration. Further, the current level increases nonlinearly with the slopes of ∼2.24 (0.3 < V < 0.56) and ∼2.08 (0.56 < V < 0.7) as the voltage increases. It verifies the SCLC (I α V^2) mechanism that suggests the charge hopping phenomenon, arising due to the halide vacancies (I_O) randomly generated across the SL facilitating the charge trapping/detrapping conduction, as shown in Figure 6b. Thereafter, the current decreases linearly while returning to 0 V with a slope of ∼1.08 (0.7 > V > 0). The ohmic conduction was then retained during a negative DC sweep until the device reached V_R = −0.44 V (Figure 6c). Afterward, ReRAM D4 switched to its HRS. Since the current largely flows through the Ag CF, it results in local joule heating, which is likely induced near the PEAI/FAI-10 interface due to the higher thermal conductivity of the PEAI layer.[52] Hence, in this case, the Ag CF ruptured at −0.44 V near the PEAI/FAI-10 interface as well as near the BE, as shown in Figure 6d.

Now, when the ReRAM D4 is illuminated under the white light, it also initially starts with a slope of ∼0.26, indicating Schottky emission (I α $V^{1/2}$) when the applied DC voltage is below 0.22 V. As the device reaches 0.22 V, it shows a discrete jump in the current level and attains its LRS. Under white light excitation, photogenerated electron−hole pairs (e^-−h^+) across the SL contributed toward higher electric field induction, which eventually led to the ReRAM set at a comparatively lower V_S of 0.22 V in comparison to the dark-condition operation. The current conduction mechanism of D4 (under white light) during the set operation is illustrated in Figure 6e. Under such a high electric field, more Ag^+ drifts across the PEAI/FAI-10 interface and consequently forms thicker Ag CF across SL (Figure 6f), which thus results in higher current under white light illumination. Later on, when the device is biased for negative DC sweep, it shows ohmic conduction with a slope of ∼1.03 (0 < V < −0.28) and returns to its HRS at −0.48 V (Figure 6g). At V_R = −0.48 V, the Ag CF ruptured at the PEAI/FAI-10 interface as well as at BE (Figure 6h), similar to the case when D4 operated under the dark condition.

At last, a crucial factor, which is the uniformity of the deposited HHP thin film, is scrutinized. The uniformity of device operation is one of the major concerns in the field of perovskite-based ReRAM devices. Since, for bulk-scale fabrication, the uniform deposition of the thin film over the platform is one of the essential requirements, the fabricated ReRAM prototype cannot be put in front of potential candidates in the field of memory devices if the uniform deposition of the switching layer cannot be obtained. Therefore, to examine the uniformity of the deposited perovskite thin film, we tested ten random devices from each of the fabricated samples: Ag/FAI-10/FTO and Ag/PEAI/FAI-10/FTO, under dark and white light illumination. Further, the cumulative distribution function (CDF) % plotted by considering the LHS/RHS ratio of each ten devices from both the samples and statistical variations (σ/μ) % were extracted, as shown in Figure 7a,b. From Figure 7a, it can be observed

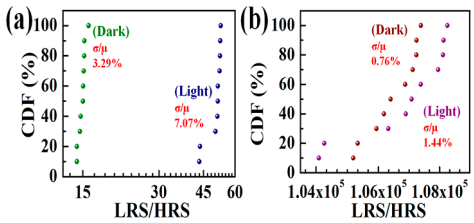

Figure 7. Device-to-device statistical variations under dark conditions and white light illumination (a) Ag/FAI-10/FTO and (b) Ag/PEAI/FAI-10/FTO.

that (σ/μ) % under dark and light illumination, respectively, are 3.29 and 7.07% for the Ag/FAI-10/FTO devices. Such minimal variations suggest that the deposition of FAI-10 HHP SL is well uniform, and therefore, each Ag/FAI-10/FTO device exhibits a nearly similar LRS/HRS ratio. When the PEAI layer was deposited over FAI-10 HHP to fabricate Ag/PEAI/FAI-10/FTO, it displayed higher accuracy and similarity when ten random devices were tested, as shown in Figure 7b, where (σ/μ) % under the dark and light, respectively, are 0.76 and 1.44%. This result suggests that the deposition of PEAI precisely filled the existing pin holes (if any) in the FAI-10 HHP and also significantly improved the perovskite thin film uniformity.

Further, a comparison has been made with the recent works on hybrid halide perovskite-based ReRAM devices presented in Table 3 to further assert the newly fabricated ReRAM device. The comparative study suggests the current work, i.e., PEAI/$MAFAPbI_3$ (with 10% FAI doping)-based ReRAM, is a potential candidate for low-voltage and low-power operable electrically and optically nonvolatile memory applications.

3. CONCLUSIONS

In summary, we have successfully optimized the FA^+ cation doping by incorporating 0 to 30% FAI into the $MAPbI_3$ perovskite solution to obtain improved $MAFAPbI_3$ SL for ReRAM. This study considered various important aspects, including morphology, GS/GB, and resistive switching proper-

https://doi.org/10.1021/acsaelm.4c00257
ACS Appl. Electron. Mater. 2024, 6, 2709−2719

Table 3. Comparison of This Work with Previously Reported Hybrid Halide Perovskite-Based ReRAM Devices[a]

perovskite	under dark condition				under light illumination				ref
	P/W (mW)	V_S (V)	V_R (V)	cycles	P/W (mW)	V_S (V)	V_R (V)	cycles	
$MAPbI_{3-X}Cl_X$		1.47	−1.41	∼50		0.1	−0.45	∼400	55
$FAPbI_3$	0.22	0.2	−0.24	∼1200					56
$MAPbI_3$	0.7	0.7	−0.7	∼400					57
$CsBi_3I_{10}$	1.7	−1.7	0.9	∼150					58
$MAPbI_3$		0.6	−1.3	∼1500		0.6	−2.0	∼1100	25
$FAPbI_3$		0.7	−2.4	∼1200		0.5	−1.7	∼800	25
$MAFAPbI_3$		0.5	−1.7	∼1300		0.3	−0.7	∼1200	25
$CsMAFAPbI_3$		0.2	−0.7	∼5000		0.2	−2.1	∼1800	25
[CNBmim]Cl/α-$FAPbI_3$	45.17 (pJ)	1	2	∼550	3.43 (pJ)	<1	<2	∼500	14
$PEAI/MAFAPbI_3$	0.12	0.26	−0.44	4003	0.23	0.22	−0.48	2436	this work

[a]P/W = power consumption; V_S = SET voltage; V_R = RESET voltage.

ties such as operating voltages, the LRS/HRS ratio, and cycle-to-cycle switching variability, to understand the influence of FAI doping percentage in the A′-site of the $AA'PbI_3$ perovskite structure. The RS characteristics have been systematically investigated for the $Ag/MAFAPbI_3/FTO$ ReRAM devices. The double-cation MA/FA at an optimized ratio provides better resistive behavior with respect to the counterparts. Also, the optimized 10% FAI-doped $Ag/MAFAPbI_3/FTO$ structures switched to LRS from HRS at 0.18 and also showed <10% variability in consecutive switching cycles while maintaining a LRS/HRS ratio of 15.2, i.e., a one-order memory window. Additionally, it offers improved resistive states and a 3.66 times higher memory window at low power, i.e., ∼0.101 mW operations under white light illumination, which confirms its candidature for optically active nonvolatile memories. The durability of the fabricated ReRAM device structures comprising $MAFAPbI_3$ (10% FAI) SL was tested, and it holds a LRS/HRS ratio of 15.2 (under dark conditions) and 54.3 (under white light) remarkably for $\sim 10^4$ s retention. Later, the PEAI passivation layer was deposited over the optimized SL, which improves the LRS/HRS to $\sim 10^5$, which is ∼6578 times higher than the $MAFAPbI_3$ (10% FAI) SL-based ReRAM configuration operated at 0.12 mW under dark conditions. Meanwhile, it exhibited ∼1841 times higher LRS/HRS when tested under white light illumination and consumed only 0.23 mW of power for reliable operations. Thus, the present work sheds light on integrating the strategies of double-cation HHP optimization with passivation layer incorporation over the optimized SL for improved RS performance toward obtaining controlled and stable RS for their potential low-power optoelectronic applications in neuromorphic computing and optoelectronic memory technology.

4. EXPERIMENTAL SECTION

4.1. Materials. Lead iodide (PbI_2, >97%), formamidinium iodide (FAI, >99%), and methylammonium hydroiodide (MAI, >99%) were purchased from Tokyo Chemical Industry (TCI). *N*,*N*-Dimethylformamide (DMF, anhydrous 99.9%), dimethyl sulfoxide (DMSO, anhydrous 99.9%), and phenethylammonium iodide (PEAI) were purchased from Sigma-Aldrich. These materials were used as such without further purification.

4.2. Perovskite Solution Preparations. First, $MAPbI_3$ and FAI solutions were prepared separately. $MAPbI_3$ solution was prepared by dissolving 1.3 mM MAI and 1.14 mM PbI_2 into the mixture of DMF/DMSO (9:1), and FAI solution was prepared by dissolving 1.3 mM FAI into the mixture of DMF/DMSO (9:1). Both solutions were dissolved for 2 h at 50 °C under constant stirring. Afterward, the required percentage amount of FAI solution was added to the prepared $MAPbI_3$ solution to obtain a perovskite formulation with 0% FAI doping, 10% FAI doping, and 30% FAI doping. The obtained perovskite formulations are $MAPbI_3$ (0% FAI), $MAFAPbI_3$ (10% FAI), and $MAFAPbI_3$ (30% FAI). For the preparation of PEAI solution, 0.25 mM PEAI salt was dissolved in IPA for 4 h. All preparations performed in the argon environment were maintained inside the glovebox.

4.3. Device Fabrication. FTO-coated glasses were sequentially cleaned in deionized (DI) water, acetone, and isopropyl alcohol through 15 min of sonication for each and then treated using UV/O_3 for 30 min. To obtain the required HHP films, the prepared precursor solutions were spin-coated on a cleaned FTO-coated glass substrate at 3000 rpm for 20 s. Toluene was used as an antisolvent during spin-coating and dropped at 10 s for each HHP spin coating to facilitate crystallization. Then, the spin-coated HHP films were annealed at 120 °C for 30 min and achieved ∼320 nm film thickness. All these spin-coating processes were performed in an argon environment inside the glovebox. Finally, Ag electrodes of ∼60 nm thickness were deposited over spin-coated HHP films through the shadow mask by using a thermal evaporator to obtain ReRAM device structures with 0.0025 cm^2 area. The passivation was performed over the $MAFAPbI_3$ HHP film by coating PEAI at 5000 rpm for 45 s and was treated at 35 °C for 60 min under argon environment. The obtained passivation layer thickness was measured at ∼20 nm. The coated PEAI layer was treated at only 35 °C to prevent its transformation into PEA_2PbI_4.[38]

■ ASSOCIATED CONTENT

Supporting Information

The Supporting Information is available free of charge at https://pubs.acs.org/doi/10.1021/acsaelm.4c00257.

AFM micrographs of nonpassivated FAI-0, FAI-10, and FAI-30 HHP thin films and their roughness data; UV−vis absorption spectra of the optimized FAI-10 HHP compared with FAI-0 HHP; endurance data of D2 ReRAM under the dark and light conditions; ReRAM performance of fabricated Pt/FAI-10/FTO and its conduction mechanism; FESEM image and AFM micrographs of PEAI-passivated FAI-10 HHP thin film; and endurance performance of D4 ReRAM under the dark and light conditions (PDF)

■ AUTHOR INFORMATION

Corresponding Author

Satinder K. Sharma − *School of Computing & Electrical Engineering (SCEE), Indian Institute of Technology (IIT) Mandi, Mandi 175075 Himachal Pradesh, India;* orcid.org/0000-0001-9313-5550; Email: satinder@iitmandi.ac.in

https://doi.org/10.1021/acsaelm.4c00257
ACS Appl. Electron. Mater. 2024, 6, 2709−2719

Authors

Manvendra Chauhan − *School of Computing & Electrical Engineering (SCEE), Indian Institute of Technology (IIT) Mandi, Mandi 175075 Himachal Pradesh, India*

Ranbir Singh − *School of Mechanical and Materials Engineering (SMME), Indian Institute of Technology (IIT) Mandi, Mandi 175075 Himachal Pradesh, India*

Complete contact information is available at: https://pubs.acs.org/10.1021/acsaelm.4c00257

Notes

The authors declare no competing financial interest.

■ ACKNOWLEDGMENTS

The authors acknowledge the Centre for Design and Fabrication of Electronic Devices (C4DFED), a Class 100 cleanroom facility available at the Indian Institute of Technology (IIT) Mandi, MANDI (Himachal Pradesh), India, for sample preparation, as well as electrical characterization facilities, an AFM and FESEM facility for nanoscale cross-section imaging.

■ REFERENCES

(1) Ding, G.; Han, S. T.; Kuo, C. C.; Roy, V. A. L.; Zhou, Y. Porphyrin-Based Metal-Organic Frameworks for Neuromorphic Electronics. *Small Struct.* **2023**, *4* (2), 2200150.

(2) Ding, G.; Zhao, J. Y.; Zhou, K.; Zheng, Q.; Han, S. T.; Peng, X.; Zhou, Y. Porous Crystalline Materials for Memories and Neuromorphic Computing Systems. *Chem. Soc. Rev.* **2023**, *52* (20), 7071−7136.

(3) Levine, I.; Nayak, P. K.; Wang, J. T. W.; Sakai, N.; Van Reenen, S.; Brenner, T. M.; Mukhopadhyay, S.; Snaith, H. J.; Hodes, G.; Cahen, D. Interface-Dependent Ion Migration/Accumulation Controls Hysteresis in MAPbI3 Solar Cells. *J. Phys. Chem. C* **2016**, *120* (30), 16399−16411.

(4) Yoo, E.; Lyu, M.; Yun, J.; Kang, C.; Choi, Y.; Wang, L. Bifunctional resistive switching behavior in an organolead halide perovskite based Ag/$CH_3NH_3PbI_{3-x}Cl_x$/FTO structure. *J. Mater. Chem. C* **2016**, *4*, 7824−7830.

(5) Choi, J.; Park, S.; Lee, J.; Hong, K.; Kim, D. H.; Moon, C. W.; Park, G. Do; Suh, J.; Hwang, J.; Kim, S. Y.; Jung, H. S.; Park, N. G.; Han, S.; Nam, K. T.; Jang, H. W. Organolead Halide Perovskites for Low Operating Voltage Multilevel Resistive Switching. *Adv. Mater.* **2016**, *28* (31), 6562−6567.

(6) Choi, J.; Han, J. S.; Hong, K.; Kim, S. Y.; Jang, H. W. Organic-Inorganic Hybrid Halide Perovskites for Memories, Transistors, and Artificial Synapses. *Adv. Mater.* **2018**, *30* (42), 1704002.

(7) You, C.; Be, M. A. Y.; In, I. *Chapter 1 Origin of Hysteresis in Perovskite Solar Cells*; AIP Publishing LLC, 2020; Vol. *041111*.

(8) Jacobs, D. A.; Wu, Y.; Shen, H.; Barugkin, C.; Beck, F. J.; White, T. P.; Weber, K.; Catchpole, K. R. Hysteresis Phenomena in Perovskite Solar Cells: The Many and Varied Effects of Ionic Accumulation. *Phys. Chem. Chem. Phys.* **2017**, *19* (4), 3094−3103.

(9) Singh, R.; Kumar, P.; Kumar, P.; Chaudhary, S.; Kan, Z.; Sharma, V.; Sharma, S. K. Indoor Bifacial Perovskite Photovoltaics: Efficient Energy Harvesting from Artificial Light Sources. *Sol. Energy* **2023**, *264*, 112061.

(10) Kundar, M.; Bhandari, S.; Chung, S.; Cho, K.; Sharma, S. K.; Singh, R.; Pal, S. K. Surface Passivation by Sulfur-Based 2D (TEA)2PbI4 for Stable and Efficient Perovskite Solar Cells. *ACS Omega* **2023**, *8* (14), 12842−12852.

(11) Singh, R.; Kumar Shukla, V.; Parashar, M.; Sharma, V.; Kumar Sharma, S. Highly Efficient Quasi-Cubic Structured Perovskite for Harvesting Energy from Artificial Indoor LED Light Source. *Sol. Energy* **2022**, *245*, 332−339.

(12) Van Reenen, S.; Kemerink, M.; Snaith, H. J. Modeling Anomalous Hysteresis in Perovskite Solar Cells. *J. Phys. Chem. Lett.* **2015**, *6* (19), 3808−3814.

(13) Zhu, X.; Lee, J.; Lu, W. D. Iodine Vacancy Redistribution in Organic-Inorganic Halide Perovskite Films and Resistive Switching Effects. *Adv. Mater.* **2017**, *29* (29), 1700527.

(14) Tao, L.; Jiang, B.; Ma, S.; Zhang, Y.; Huang, Y.; Pan, Y.; Kong, W.; Zhang, J.; Ma, G.; Wan, H.; Ding, Y.; Dyson, P. J.; Nazeeruddin, M. K.; wang, H. 3D Trigonal FAPbI3-based Multilevel Resistive Switching Nonvolatile Memory for Artificial Neural Synapse. *SmartMat* **2023**, No. e1233.

(15) Zhu, X.; Lu, W. D. Optogenetics-Inspired Tunable Synaptic Functions in Memristors. *ACS Nano* **2018**, *12* (2), 1242−1249.

(16) Yin, L.; Huang, W.; Xiao, R.; Peng, W.; Zhu, Y.; Zhang, Y.; Pi, X.; Yang, D. Optically Stimulated Synaptic Devices Based on the Hybrid Structure of Silicon Nanomembrane and Perovskite. *Nano Lett.* **2020**, *20* (5), 3378−3387.

(17) Fang, Y.; Dong, Q.; Shao, Y.; Yuan, Y.; Huang, J. Highly Narrowband Perovskite Single-Crystal Photodetectors Enabled by Surface-Charge Recombination. *Nat. Photonics* **2015**, *9* (10), 679−686.

(18) Lee, M. M.; Teuscher, J.; Miyasaka, T.; Murakami, T. N.; Snaith, H. J. Efficient Hybrid Solar Cells Based on Meso-Superstructured Organometal Halide Perovskites. *Science* **2012**, *338* (6107), 643−647.

(19) Shi, D.; Adinolfi, V.; Comin, R.; Yuan, M.; Alarousu, E.; Buin, A.; Chen, Y.; Hoogland, S.; Rothenberger, A.; Katsiev, K.; Losovyj, Y.; Zhang, X.; Dowben, P. A.; Mohammed, O. F.; Sargent, E. H.; Bakr, O. M. Low Trap-State Density and Long Carrier Diffusion in Organolead Trihalide Perovskite Single Crystals. *Science* **2015**, *347* (6221), 519−522.

(20) Sun, C.; Wade, M. T.; Lee, Y.; Orcutt, J. S.; Alloatti, L.; Georgas, M. S.; Waterman, A. S.; Shainline, J. M.; Avizienis, R. R.; Lin, S.; Moss, B. R.; Kumar, R.; Pavanello, F.; Atabaki, A. H.; Cook, H. M.; Ou, A. J.; Leu, J. C.; Chen, Y. H.; Asanović, K.; Ram, R. J.; Popović, M. A.; Stojanović, V. M. Single-Chip Microprocessor That Communicates Directly Using Light. *Nature* **2015**, *528* (7583), 534−538.

(21) Seo, S.; Jo, S. H.; Kim, S.; Shim, J.; Oh, S.; Kim, J. H.; Heo, K.; Choi, J. W.; Choi, C.; Oh, S.; Kuzum, D.; Wong, H. S. P.; Park, J. H. Artificial Optic-Neural Synapse for Colored and Color-Mixed Pattern Recognition. *Nat. Commun.* **2018**, *9* (1), 5106.

(22) Leijtens, T.; Bush, K.; Cheacharoen, R.; Beal, R.; Bowring, A.; McGehee, M. D. Towards Enabling Stable Lead Halide Perovskite Solar Cells; Interplay between Structural, Environmental, and Thermal Stability. *J. Mater. Chem. A* **2017**, *5* (23), 11483−11500.

(23) Pellet, N.; Gao, P.; Gregori, G.; Yang, T. Y.; Nazeeruddin, M. K.; Maier, J.; Grätzel, M. Mixed-Organic-Cation Perovskite Photovoltaics for Enhanced Solar-Light Harvesting. *Angew. Chem., Int. Ed.* **2014**, *53* (12), 3151−3157.

(24) Yi, C.; Luo, J.; Meloni, S.; Boziki, A.; Ashari-Astani, N.; Grätzel, C.; Zakeeruddin, S. M.; Röthlisberger, U.; Grätzel, M. Entropic Stabilization of Mixed A-Cation ABX3Metal Halide Perovskites for High Performance Perovskite Solar Cells. *Energy Environ. Sci.* **2016**, *9* (2), 656−662.

(25) George, T.; Vadivel Murugan, A. Revealing the Effect of Substitutional Cation Doping in the A-Site of Nanoscale APbI3 Perovskite Layers for Enhanced Retention and Endurance in Optoelectronic Resistive Switching for Non-Volatile Bipolar Memory Devices. *Nanoscale* **2023**, *15* (15), 6960−6975.

(26) Yun, J. S.; Seidel, J.; Kim, J.; Soufiani, A. M.; Huang, S.; Lau, J.; Jeon, N. J.; Seok, S. Il; Green, M. A.; Ho-Baillie, A. Critical Role of Grain Boundaries for Ion Migration in Formamidinium and Methylammonium Lead Halide Perovskite Solar Cells. *Adv. Energy Mater.* **2016**, *6* (13), 1600330.

(27) Lee, D.; Hwang, B.; Lee, J. S. Impact of Grain Sizes on Programmable Memory Characteristics in Two-Dimensional Organic-Inorganic Hybrid Perovskite Memory. *ACS Appl. Mater. Interfaces* **2019**, *11* (22), 20225−20231.

(28) Park, Y.; Lee, J. S. Controlling the Grain Size of Dion-Jacobson-Phase Two-Dimensional Layered Perovskite for Memory Application. *ACS Appl. Mater. Interfaces* **2022**, *14* (3), 4371−4377.
(29) Nukunudompanich, M.; Budiutama, G.; Suzuki, K.; Hasegawa, K.; Ihara, M. Dominant Effect of the Grain Size of the MAPbI3 Perovskite Controlled by the Surface Roughness of TiO2 on the Performance of Perovskite Solar Cells. *CrystEngComm* **2020**, *22* (16), 2718−2727.
(30) Anaya Gonzalez, G. S.; Jeronimo-Rendon, J. J.; Wang, Q.; Li, G.; Alvarez, A. O.; Fabregat-Santiago, F.; Köbler, H.; Alvarado, A.; Juárez-Santiesteban, H.; Turren-Cruz, S. H.; Saliba, M.; Abate, A. Large Grain Size with Reduced Non-Radiative Recombination in Potassium Incorporated Methylammonium-Free Perovskite Solar Cells. *Sol. Energy Mater. Sol. Cells* **2022**, *248*, 111964.
(31) Kim, H. S.; Park, N. G. Importance of Tailoring Lattice Strain in Halide Perovskite Crystals. *NPG Asia Mater.* **2020**, *12* (1), 78.
(32) Wu, J.; Liu, S. C.; Li, Z.; Wang, S.; Xue, D. J.; Lin, Y.; Hu, J. S. Strain in Perovskite Solar Cells: Origins, Impacts and Regulation. *Natl. Sci. Rev.* **2021**, *8* (8), nwab047.
(33) Tsai, H.; Asadpour, R.; Blancon, J.; Stoumpos, C. C.; Durand, O.; Strzalka, J. W.; Chen, B.; Verduzco, R.; Ajayan, P. M.; Tretiak, S.; Even, J.; Alam, M. A.; Kanatzidis, M. G.; Nie, W.; Mohite, A. D. Light-Induced Lattice Expansion Leads to High-Efficiency Perovskite Solar Cells. *Science* **2018**, *360* (6384), 67−70.
(34) Wetzelaer, G. J. A. H.; Scheepers, M.; Sempere, A. M.; Momblona, C.; Ávila, J.; Bolink, H. J. Trap-Assisted Non-Radiative Recombination in Organic-Inorganic Perovskite Solar Cells. *Adv. Mater.* **2015**, *27* (11), 1837−1841.
(35) Wang, Q.; Dong, Q.; Li, T.; Gruverman, A.; Huang, J. Thin Insulating Tunneling Contacts for Efficient and Water-Resistant Perovskite Solar Cells. *Adv. Mater.* **2016**, *28* (31), 6734−6739.
(36) Kim, M.; Motti, S. G.; Sorrentino, R.; Petrozza, A. Enhanced Solar Cell Stability by Hygroscopic Polymer Passivation of Metal Halide Perovskite Thin Film. *Energy Environ. Sci.* **2018**, *11* (9), 2609−2619.
(37) Bai, Y.; Xiao, S.; Hu, C.; Zhang, T.; Meng, X.; Lin, H.; Yang, Y.; Yang, S. Dimensional Engineering of a Graded 3D-2D Halide Perovskite Interface Enables Ultrahigh Voc Enhanced Stability in the p-i-n Photovoltaics. *Adv. Energy Mater.* **2017**, *7* (20), 1701038.
(38) Jiang, Q.; Zhao, Y.; Zhang, X.; Yang, X.; Chen, Y.; Chu, Z.; Ye, Q.; Li, X.; Yin, Z.; You, J. Surface Passivation of Perovskite Film for Efficient Solar Cells. *Nat. Photonics* **2019**, *13* (7), 460−466.
(39) Zhang, F.; Huang, Q.; Song, J.; Zhang, Y.; Ding, C.; Liu, F.; Liu, D.; Li, X.; Yasuda, H.; Yoshida, K.; Qu, J.; Hayase, S.; Toyoda, T.; Minemoto, T.; Shen, Q. Growth of Amorphous Passivation Layer Using Phenethylammonium Iodide for High-Performance Inverted Perovskite Solar Cells. *Sol. RRL* **2020**, *4* (2), 1900243.
(40) Lanza, M.; Zhang, K.; Porti, M.; Nafría, M.; Shen, Z. Y.; Liu, L. F.; Kang, J. F.; Gilmer, D.; Bersuker, G. Grain Boundaries as Preferential Sites for Resistive Switching in the HfO 2 Resistive Random Access Memory Structures. *Appl. Phys. Lett.* **2012**, *100* (12), 123508.
(41) Yuan, Y.; Huang, J. Ion Migration in Organometal Trihalide Perovskite and Its Impact on Photovoltaic Efficiency and Stability. *Acc. Chem. Res.* **2016**, *49* (2), 286−293.
(42) Geske, T.; Li, J.; Worden, M.; Shan, X.; Chen, M.; Bade, S. G. R.; Yu, Z. Deterministic Nucleation for Halide Perovskite Thin Films with Large and Uniform Grains. *Adv. Funct. Mater.* **2017**, *27* (40), 1702180.
(43) Thien, G. S. H.; Sarjidan, M. A. M.; Talik, N. A.; Goh, B. T.; Yap, B. K.; He, Z.; Chan, K. Y. Electrode Dependence in Halide Perovskite Memories: Resistive Switching Behaviours. *Mater. Chem. Front.* **2022**, *6* (21), 3125−3142.
(44) Choudhary, S.; Soni, M.; Sharma, S. K. Low Voltage & Controlled Switching of MoS2-GO Resistive Layers Based ReRAM for Non-Volatile Memory Applications. *Semicond. Sci. Technol.* **2019**, *34* (8), 085009.
(45) Muthu, C.; Resmi, A. N.; Pious, J. K.; Dayal, G.; Krishna, N.; Jinesh, K. B.; Vijayakumar, C. Resistive Switching in Formamidinium Lead Iodide Perovskite Nanocrystals: A Contradiction to the Bulk Form. *J. Mater. Chem. C* **2021**, *9* (1), 288−293.
(46) George, T.; Murugan, A. V. Improved Performance of the Al2O3-Protected HfO2-TiO2Base Layer with a Self-Assembled CH3NH3PbI3Heterostructure for Extremely Low Operating Voltage and Stable Filament Formation in Nonvolatile Resistive Switching Memory. *ACS Appl. Mater. Interfaces* **2022**, *14* (45), 51066−51083.
(47) Sharma, S.; Kumar, A.; Dutta, S.; Kaur, D. Optically Triggered Multilevel Resistive Switching Characteristics of Cu/MoS2/AlN/ITO Bilayer Memory Structure. *Appl. Phys. Lett.* **2020**, *117* (19), 192101.
(48) Hsu, C.-C.; Long, P.-X.; Lin, Y. S.; Long, P.; Lin, Y. Enhancement of Resistive Switching Characteristics of Sol−Gel TiO_x RRAM Using Ag Conductive Bridges. *IEEE Trans. Electron Devices* **2021**, *68* (1), 95−102.
(49) Zhang, Y.; Poddar, S.; Huang, H.; Gu, L.; Zhang, Q.; Zhou, Y.; Yan, S.; Zhang, S.; Song, Z.; Huang, B.; et al. Three-Dimensional Perovskite Nanowire Array - Based Ultrafast Resistive RAM with Ultralong Data Retention. *Sci. Adv.* **2021**, *7*, No. eabg3788.
(50) Paramanik, S.; Maiti, A.; Chatterjee, S.; Pal, A. J. Large Resistive Switching and Artificial Synaptic Behaviors in Layered Cs3Sb2I9 Lead-Free Perovskite Memory Devices. *Adv. Electron. Mater.* **2022**, *8* (1), 1−10.
(51) Wang, Y.; Lv, Z.; Liao, Q.; Shan, H.; Chen, J.; Zhou, Y.; Zhou, L.; Chen, X.; Roy, V. A. L.; Wang, Z.; Xu, Z.; Zeng, Y. J.; Han, S. T. Synergies of Electrochemical Metallization and Valance Change in All-Inorganic Perovskite Quantum Dots for Resistive Switching. *Adv. Mater.* **2018**, *30* (28), 1800327.
(52) Lee, S. M.; Kim, H.; Kim, D. H.; Kim, W. B.; Lee, J. M.; Choi, J.; Shin, H.; Han, G. S.; Jang, H. W.; Jung, H. S. Tailored 2D/3D Halide Perovskite Heterointerface for Substantially Enhanced Endurance in Conducting Bridge Resistive Switching Memory. *ACS Appl. Mater. Interfaces* **2020**, *12* (14), 17039−17045.
(53) Seo, J. Y.; Choi, J.; Kim, H. S.; Kim, J.; Yang, J. M.; Cuhadar, C.; Han, J. S.; Kim, S. J.; Lee, D.; Jang, H. W.; Park, N. G. Wafer-Scale Reliable Switching Memory Based on 2-Dimensional Layered Organic-Inorganic Halide Perovskite. *Nanoscale* **2017**, *9* (40), 15278−15285.
(54) Chauhan, M.; Choudhary, S.; Sharma, S. K. Reliable Memristive Switching Empowered by Ag/NiO/W ReRAM Configuration for Multi-Level Non-Volatile Memory Applications. *Adv. Electron. Mater.* **2024**, 2300724.
(55) Zhou, F.; Liu, Y.; Shen, X.; Wang, M.; Yuan, F.; Chai, Y. Low-Voltage, Optoelectronic CH3NH3PbI3-xClx Memory with Integrated Sensing and Logic Operations. *Adv. Funct. Mater.* **2018**, *28* (15), 1800080.
(56) Yang, J. M.; Kim, S. G.; Seo, J. Y.; Cuhadar, C.; Son, D. Y.; Lee, D.; Park, N. G. 1D Hexagonal HC(NH2)2PbI3 for Multilevel Resistive Switching Nonvolatile Memory. *Adv. Electron. Mater.* **2018**, *4* (9), 1−9.
(57) Gu, C.; Lee, J. S. Flexible Hybrid Organic-Inorganic Perovskite Memory. *ACS Nano* **2016**, *10* (5), 5413−5418.
(58) Xiong, Z.; Hu, W.; She, Y.; Lin, Q.; Hu, L.; Tang, X.; Sun, K. Air-Stable Lead-Free Perovskite Thin Film Based on CsBi3I10 and Its Application in Resistive Switching Devices. *ACS Appl. Mater. Interfaces* **2019**, *11* (33), 30037−30044.

https://doi.org/10.1021/acsaelm.4c00257
ACS Appl. Electron. Mater. 2024, 6, 2709−2719